JOURNAL OF SPACECRAFT AND ROCKETS
Vol. 34, No. 3, May–June 1997

Unsteady Flowfield and Cavity Acoustics of the Stratospheric Observatory for Infrared Astronomy

G. R. Srinivasan*
NASA Ames Research Center, Moffett Field, California 94035-1000

The Stratospheric Observatory for Infrared Astronomy is a 2.5-m-aperture Cassegrain telescope housed in an open cavity onboard a Boeing 747 aircraft. This flying observatory operates in the Earth's stratosphere, at an altitude above 12.5 km, to view objects in the universe in the infrared region of the electromagnetic spectrum. The location of the telescope in an open cavity during its operation presents some challenging aerodynamic and aeroacoustic problems. A combined computational fluid dynamics (CFD) and experimental investigation has been initiated to understand and resolve these issues. Different aircraft platforms, cavity apertures, aft ramp shapes, and telescope configurations have been considered in these studies. The present study focuses on the findings from a CFD study of a circular aperture cavity in the Boeing 747-200 aircraft platform and a tub telescope. In particular, numerical solutions of Navier–Stokes equations on overset grid systems are presented at wind-tunnel and cruise flight conditions for a freestream condition of $M_\infty = 0.85$ and $\alpha = 2.5$ deg. Comparison of CFD results for wind-tunnel conditions show good agreement with experimental data for drag and time-averaged surface pressures and fair agreement for sound pressure levels and power spectra at various locations within the cavity and on the telescope. The open-cavity condition produces an increase in drag of 2%. However, the open-cavity impact on the effectiveness of aircraft control surfaces appears minimal.

Nomenclature

a	= local speed of sound
a_∞	= freestream speed of sound, characteristic velocity scale
b	= semispan of horizontal tail
C_D	= drag coefficient, $D/q_\infty S$
C_L	= lift coefficient, $L/q_\infty S$
C_p	= pressure coefficient based on freestream dynamic pressure
D	= drag
Dt	= nondimensional time step, dta_∞/l
dt	= physical time step
$\hat{E}, \hat{F}, \hat{G}$	= inviscid flux vectors
e	= energy per unit volume
h_c	= cavity depth
L	= lift; length of aircraft
l	= characteristic length scale
l_c	= cavity aperture width in x direction
M_∞	= freestream Mach number
p	= fluid pressure
$\hat{Q}$	= vector of conserved flow quantities
q_∞	= freestream dynamic pressure
Re	= Reynolds number
S	= wing planform area
$\hat{S}$	= viscous flux vector
U, V, W	= contravariant velocity components
u, v, w	= velocity components in physical space
X, Y, Z	= telescope coordinates (see Fig. 9)
x, y, z, t	= physical space coordinates
α	= angle of attack, degrees
γ	= ratio of specific heats
ρ	= density
ξ, η, ζ, τ	= body-conforming coordinates in computational space

Received May 18, 1995; presented as Paper 95-1862 at the AIAA 13th Applied Aerodynamics Conference, San Diego, CA, June 19–22, 1995; revision received March 7, 1997; accepted for publication March 7, 1997.

*Senior Research Scientist, Sterling Software. Associate Fellow AIAA.

Introduction

THE Stratospheric Observatory for Infrared Astronomy (SOFIA) is a 2.5-m-aperture Cassegrain telescope, with a Nasmyth focus, housed in a Boeing 747 aircraft. It will fly in the Earth's stratosphere, between 12.5- and 13.7-km altitude, to view celestial objects in the universe in the infrared region of the electromagnetic spectrum. At this altitude, in the clear, dry environment (free of water vapor) on the edge of space, SOFIA will enable researchers to study radiant heat patterns from stars, planets, and other celestial sources. It is a joint mission of NASA and the German Space Agency, DARA. SOFIA is a follow-on mission to NASA's Kuiper Airborne Observatory (KAO) that was decommissioned in 1995. When it becomes operational, SOFIA will posses capabilities significantly greater than the KAO and offer advantages over other Earth- and space-based instruments.

The use of an airborne telescope housed in a moving platform, shown in an artist's rendition in Fig. 1, offers many advantages over a land-based system. In particular, the attenuation and/or absorption of wavelengths of interest by the water vapor in the Earth's atmosphere will be avoided by using a system placed above the tropopause. However, the moving aircraft-based observatory poses problems of a different nature. As noted in earlier studies, the telescope-housing cavity poses complex unsteady fluid dynamic problems if left untreated.[1] Experimental observations have shown violent shear-layer oscillations accompanied by dangerous levels of noise.[2–4] In fact, the open-cavity environment creates several challenging aerodynamic and aeroacoustic design problems. Foremost among these are as follows. The uncontrolled shear layer will produce unwanted cavity resonance and sound pressure levels (SPL); the unsteady flow within the cavity will produce large dynamic loads and moments on the telescope and thus will impact its pointing accuracy; the open-cavity environment and shear-layer control devices will produce increased drag, which will directly affect the time of flight of the mission; and the fatigue life of aircraft as well as the effectiveness of aircraft control surfaces also are influenced by the unsteady flow.

There have been many experimental and computational investigations in the literature on the driven cavity flow problem.[5–11] The cavity geometry in these investigations varies from a simple two-dimensional cavity to more complex three-dimensional cavities. Many studies among these investigations address the issue of cavity acoustics from the point of aircraft store separation. Although some of the fluid flow issues in the present investigation are similar in nature, the impact of an open cavity in flight brings additional

Fig. 1 Artist's rendition of SOFIA in flight.

problems noted earlier. To understand and resolve these problems in SOFIA, extensive wind-tunnel testing has been done in the past few years to assist in the design of a nonresonant cavity for the telescope using Boeing 747-SP and 747-200 aircraft platforms.[2–4] The primary goal of these investigations was to identify a shear-layer control scheme that provided lowest possible sound pressure levels and a nearly nonresonant cavity environment. Some of the early developmental research done on KAO[12,13] is not directly useful in the SOFIA developmental program because of differences in aircraft platform, cavity location, aperture size and shape, telescope configuration, and cruise flight conditions.

The investigation of the aerodynamic and acoustic issues pertinent to the SOFIA design has progressed utilizing both wind-tunnel testing and computational simulations. There is a continuing emphasis on this two-pronged attack to arrive at a final configuration for the cavity, the aperture shape, and finally the telescope itself. Just like in KAO, the cavity location in SOFIA started out on the forward section of fuselage behind the cockpit but was later moved to a more favorable downstream location behind the portside wing. Both the forward- and aft-located cavity configurations were the subject of the first Navier–Stokes investigations undertaken by Atwood.[14–16] The configurations were investigated used a sting-mounted 7% wind-tunnel scale model of the Boeing 747-SP aircraft without an empennage. The model used a tub telescope and a circular aperture for the cavity. Subsequent computational investigations used similar scale models with complete empennage. A brief summary of the findings from these investigations is described by Machak et al.[17]

The computational fluid dynamics (CFD) simulations not only complement the experimental database but also provide detailed flowfield information that is hard to duplicate in a wind-tunnel test. The present investigation is one such study in this direction to evaluate the feasibility of using a Boeing 747-200 aircraft as an alternative platform for the SOFIA. Although, this computational investigation is the first one using a Boeing 747-200 aircraft as a platform for SOFIA, it will complement other CFD investigations carried out using a Boeing 747-SP aircraft by Atwood[14–16] and Klotz.[18] The location of the cavity, its proximity to the empennage surface, and the difference in the geometries of the two aircraft will bring out similarities to and/or differences between the two concepts.

Governing Equations and Solution Method

The governing differential equations are the thin-layer Navier–Stokes equations. These can be written in conservation-law form in a generalized body-conforming curvilinear coordinate system as follows[19]:

$$\partial_\tau \hat{Q} + \partial_\xi \hat{E} + \partial_\eta \hat{F} + \partial_\zeta \hat{G} = (1/Re)\partial_\zeta \hat{S} \tag{1}$$

where $\xi = \xi(x, y, z, t)$, $\eta = \eta(x, y, z, t)$, $\zeta = \zeta(x, y, z, t)$, and $\tau = t$; (x, y, z, t) is the inertial coordinate system. The vector of conserved flow quantities $\hat{Q}$ and the inviscid flux vectors $\hat{E}$, $\hat{F}$, and $\hat{G}$ are given by

$$\hat{Q} = \frac{1}{J}\begin{bmatrix} \rho \\ \rho u \\ \rho v \\ \rho w \\ e \end{bmatrix}, \qquad \hat{E} = \frac{1}{J}\begin{bmatrix} \rho U \\ \rho u U + \xi_x p \\ \rho v U + \xi_y p \\ \rho w U + \xi_z p \\ U H - \xi_t p \end{bmatrix}$$

$$\hat{F} = \frac{1}{J}\begin{bmatrix} \rho V \\ \rho u V + \eta_x p \\ \rho v V + \eta_y p \\ \rho w V + \eta_z p \\ V H - \eta_t p \end{bmatrix}, \qquad \hat{G} = \frac{1}{J}\begin{bmatrix} \rho W \\ \rho u W + \zeta_x p \\ \rho v W + \zeta_y p \\ \rho w W + \zeta_z p \\ W H - \zeta_t p \end{bmatrix} \tag{2}$$

In these equations, $H = (e + p)$ and U, V, and W are the contravariant velocity components defined, for example, as $U = \xi_t + \xi_x u + \xi_y v + \xi_z w$. The Cartesian velocity components are given by u, v, and w in the x, y, and z directions, respectively. The coordinate x is along aircraft longitudinal axis, viz., along fuselage length from nose to tail; y is perpendicular to this and toward the starboard wing; and z points in the vertical direction (positive upward). All velocities and lengths are nondimensionalized by the ambient sound speed a_∞ and unit length scale. The pressure p, density ρ, and the energy e are nondimensionalized by the freestream reference values p_∞/γ, ρ_∞, and $\rho_\infty a_\infty^2$, respectively. The quantities $\xi_x, \xi_y, \xi_z, \xi_t$, etc., are the coordinate transformation metrics and J is the determinant of the transformation Jacobian. For the thin-layer approximation used here, the viscous flux vector $\hat{S}$ is given by

$$\hat{S} = \frac{1}{J}\begin{bmatrix} 0 \\ \mu m_1 u_\zeta + (\mu/3) m_2 \zeta_x \\ \mu m_1 v_\zeta + (\mu/3) m_2 \zeta_y \\ \mu m_1 w_\zeta + (\mu/3) m_2 \zeta_z \\ \mu m_1 m_3 + (\mu/3) m_2 (\zeta_x u + \zeta_y v + \zeta_z w) \end{bmatrix} \tag{3}$$

with

$$m_1 = \zeta_x^2 + \zeta_y^2 + \zeta_z^2, \qquad m_2 = \zeta_x u_\zeta + \zeta_y v_\zeta + \zeta_z w_\zeta$$

$$m_3 = \frac{1}{2}(u^2 + v^2 + w^2)_\zeta + \frac{1}{Pr\,(\gamma - 1)}(a^2)_\zeta$$

where Pr is the Prandtl number. The fluid pressure p is related to the conserved flow quantities through the nondimensional equation of state for a perfect gas given by

$$p = (\gamma - 1)[e - (\rho/2)(u^2 + v^2 + w^2)] \tag{4}$$

The numerical method solves the Reynolds-averaged Navier–Stokes equations on an overset grid framework using the flow solver OVERFLOW.[20] This flow solver uses a central-difference, implicit, diagonal algorithm[21] with added second- and fourth-order numerical dissipation. The numerical scheme is second-order accurate in space and first-order accurate in time. For turbulent viscous flows, the nondimensional viscosity coefficient μ in $\hat{S}$ is computed as a sum of $\mu_l + \mu_t$, where the laminar viscosity μ_l is estimated using Sutherland's law and the turbulent viscosity μ_t is evaluated using the Baldwin–Lomax algebraic eddy viscosity model.[22] In the present computations the boundary layer along the entire aircraft is assumed to be fully turbulent. The eddy viscosity in the shear layer, however, is computed as outlined by Buning and Chan[20] using a shear-layer model. Note that the feature of cavity resonance is not strongly dependent on the turbulence model used in the cavity.[14] The boundary conditions are applied explicitly. A no-slip boundary condition is specified at the wall with zero normal pressure gradient along with an adiabatic wall condition. At far field, characteristic boundary conditions are specified. To update the information exchange at the overset grid interface, a trilinear interpolation of the dependent variables is used. The computations were performed on the Numerical Aerodynamic Simulation and

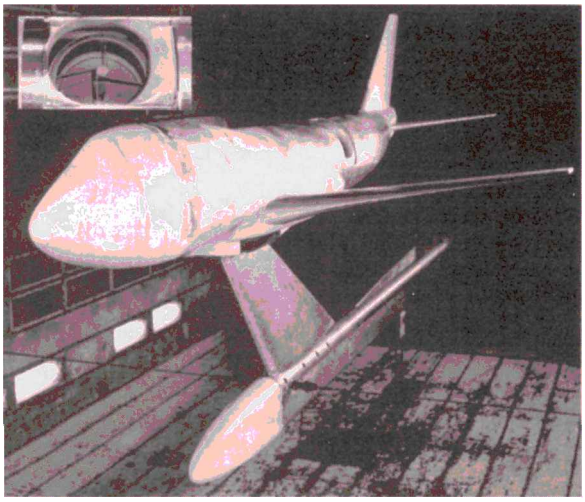

Fig. 2 Wind-tunnel 7% scale model of Boeing 747-200 aircraft, showing the aft-located cavity and tub telescope.

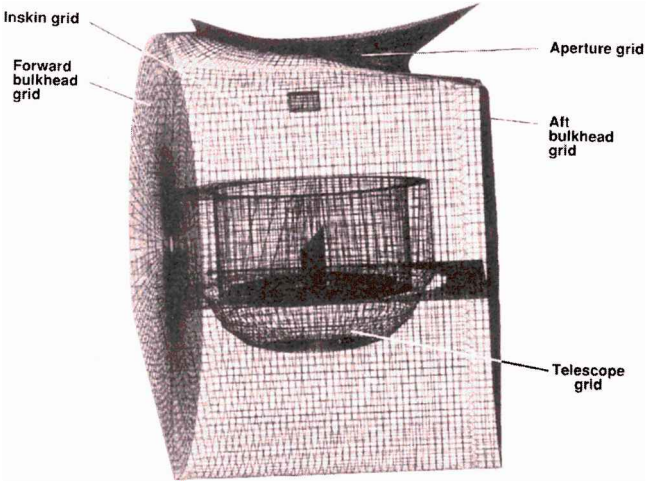

Fig. 3 View of the cavity and telescope surface grids.

Aeronautics Consolidated Supercomputing Facility Cray C-90 supercomputers at the NASA Ames Research Center. The flow solver cost is 6.7 μs/iteration per grid point on these supercomputers for the algorithm options described.

The construction of surface geometry of the Boeing 747-200 aircraft configuration uses several computational tools. Initially, the surface grids were constructed from the computer-aided design (CAD) surface data using the GRIDGEN2D[23] and S3D[24] grid generation tools. Because the wind-tunnel model and cruise flight configurations were different, two separate surface geometries had to be constructed. The cruise flight simulation used powered engines (engine pylons were not modeled), whereas the wind-tunnel configuration had no engines and its wings were clipped (for smaller span). With this difference in the two configurations, the cruise flight model had 45 overset grids and the wind-tunnel model had 29 overset grids. This included seven grids for the cavity and telescope assembly in each case. Figure 2 shows the 7% wind-tunnel scale model with circular aperture cavity and telescope assembly. Figure 3 shows the surface grid of the cavity and tub-telescope assembly, as modeled in the present study. With all surface overset grids in place, structured volume grids of O-O, C-O, and H-H topology were constructed using the HYPGEN hyperbolic grid generator.[25] The spacing of the first grid point from the surface in these grids varied from grid to grid and was between $2 \times 10^{-5}l$ to $5 \times 10^{-5}l$. A measure of a grid's ability to resolve the viscous layer is indicated by the y^+ value. The grids used in this study have a $y^+ = 1.0$–2.1 over the entire grid range. Grids so constructed had 2.7 million and 4.1 million grid points, for the clean and cavity/telescope configurations, respectively.

Once the volume grids are in place in the overset grid framework, the next step is to create proper hole boundaries in individual grids. This is achieved by running the PEGSUS code.[26,27] Creating proper hole shape and boundaries is an iterative process and requires several iterations of hole cutting and (surface and volume) grid generation to eliminate all orphan points in the flowfield. Although tedious, the Chimera hole creation job is a necessary step in the overall solution process of such complex configurations. More information on individual grids and Chimera hole boundaries is given elsewhere.[28]

Results and Discussion

Numerical results from two CFD calculations, one corresponding to the full-configuration free-flight (F-F) condition and the other to the wind-tunnel (W-T) condition, are presented. Both calculations are performed for a cruise flight Mach number of $M_\infty = 0.85$ and an angle-of-attack $\alpha = 2.5$ deg. The F-F condition corresponds to cruise at 12.5-km altitude with powered engines (power setting is done via boundary-condition procedure). The Reynolds number at this altitude for the full-scale aircraft is $Re = 4.72 \times 10^5$/m. As mentioned before, the wind-tunnel model used a slightly different configuration from the F-F case. It had no engines and its wings were clipped (for smaller span) to accommodate the model in the 4.3-m (14-ft) wind tunnel at the NASA Ames Research Center. The wind-tunnel calculations used a Reynolds number $Re = 1.22 \times 10^6$/m. Wind-tunnel walls were not included in any of the CFD calculations.

Figure 2 shows a view of the wind-tunnel model with an aft-located cavity and tub-telescope. The location of the telescope cavity and its geometry are identical for the two calculations. The aperture has a smooth aft ramp downstream of the cavity for shear-layer control. The telescope geometry, shown in Fig. 3, is a simplified version of the telescope used in the wind-tunnel model shown in Fig. 2. As shown in Fig. 3, the cavity is isolated from the pressurized aircraft cabin by means of forward and aft bulkheads.

Unsteady calculations are run starting from an initial quasisteady solution with a constant nondimensional time step of $Dt = 0.11$. This time step translates to 136 μs of real time at cruise flight and 9.5 μs at the wind-tunnel test conditions. This value of dt is the stability-limited time-step size. However, the cavity grids, including the shear-layer grid, used a $dt = 3.17$ μs. This time-step size corresponds to a Courant–Friedrichs–Lewy (CFL) value of about 1 in the streamwise direction within the shear layer, and a $\mathrm{CFL}_{\max} \simeq 500$. Unsteady data were collected for a duration of 1.5 s real time in cruise flight and 0.13 s real time in the wind tunnel. By comparison, the wind-tunnel test data trace is 5 s. The numerical calculations are time-consuming and a typical CFD solution required about 100 Cray C-90 CPU hours, which includes the initial quasisteady calculations.

A comparison of steady surface pressure coefficients on fuselage and wing for the clean configuration shows good agreement with experiments, and the results are reported elsewhere.[28] A comparison of unsteady pressures is presented here. Time-averaged surface pressure coefficients on the horizontal and vertical tails are presented in Fig. 4 and compared with time-averaged experimental data. Considering the short duration data-trace for computed results compared to 5-s-duration data for experiments, the agreement between calculation and experiment is very good, although some data stations show some discrepancy. A detailed inspection of surface pressures and surface oil flow on both port and starboard side of the tail indicate no flow separation on the entire tail surface. This indicates that the open-cavity environment does not produce any detrimental effect for the aircraft control surfaces. Figure 5 shows a map of instantaneous (snapshot) picture of the unsteady surface pressure coefficient C_p for the full aircraft at F-F cruise condition. The surface color map shows a variation of C_p according to the noted color scale, with red indicating high pressures and blue for low pressures. The cavity aft bulkhead region is seen as a region of high pressure followed by a small region of flow expansion on the ramp of the cavity aperture. Inspection of a map of instantaneous Mach number contours within the cavity show a slow recirculating flow of Mach number $M \leq 0.1$, except for a few hot-spot locations in the corners of the cavity and tub-telescope.

Table 1 compares computed and experimental SPL on the telescope and bulkheads at pressure tap locations shown in Fig. 6. Generally, the CFD calculations underpredict experimental SPL at most locations in the cavity. Inspection of power spectra density (PSD)

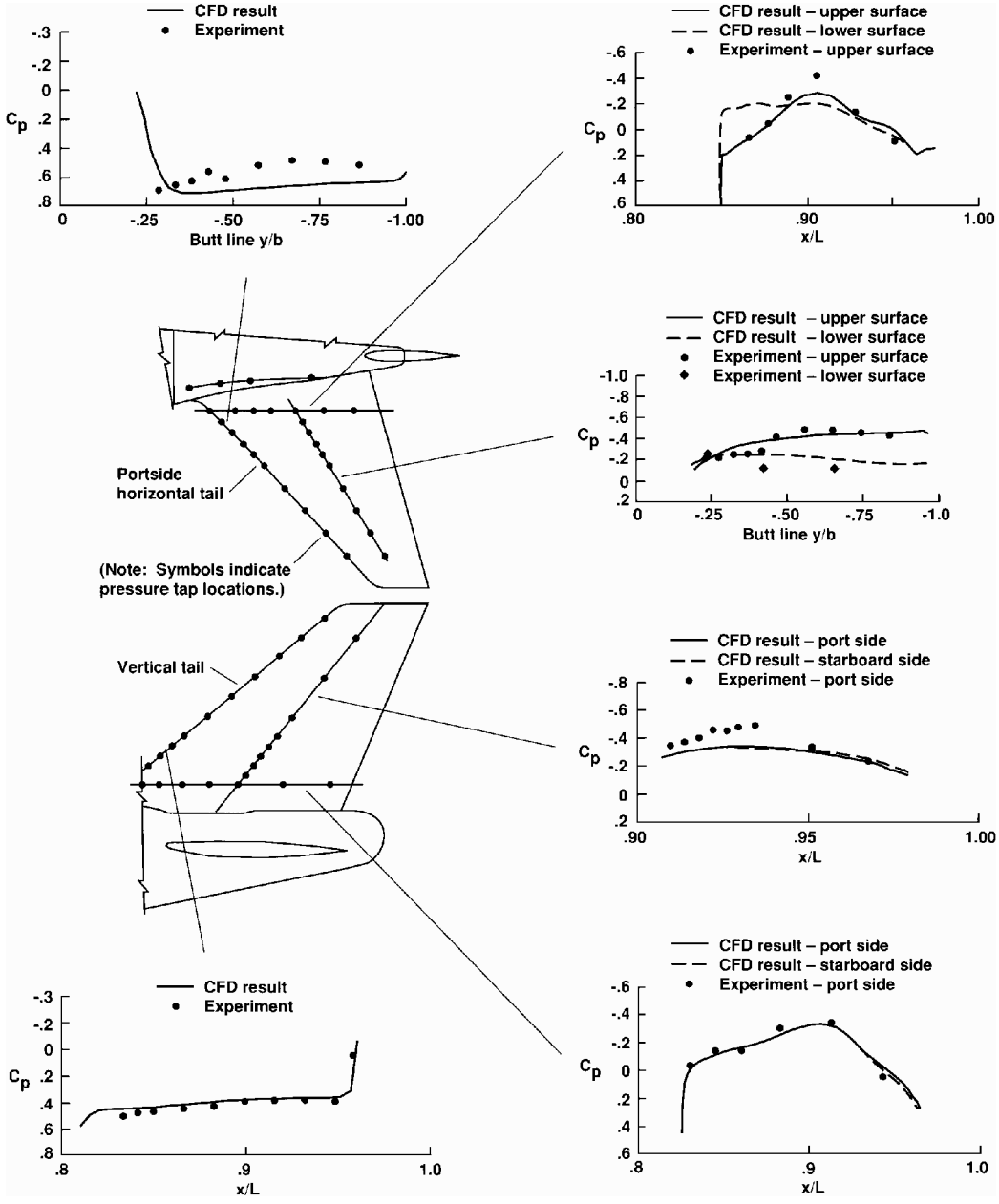

Fig. 4 Comparison of computed and experimental time-averaged surface pressure coefficients on vertical and horizontal tails at wind-tunnel conditions $M_{tip} = 0.85$, $\alpha = 2.5$ deg, and $Re = 1.22 \times 10^6$/m.

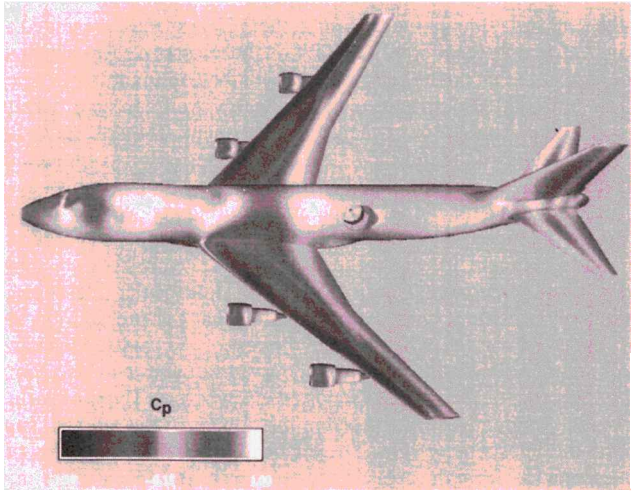

Fig. 5 Instantaneous surface pressure C_p map for full-configuration F-F conditions $M_{tip} = 0.85$, $\alpha = 2.5$ deg, and $Re = 4.72 \times 10^5$/m.

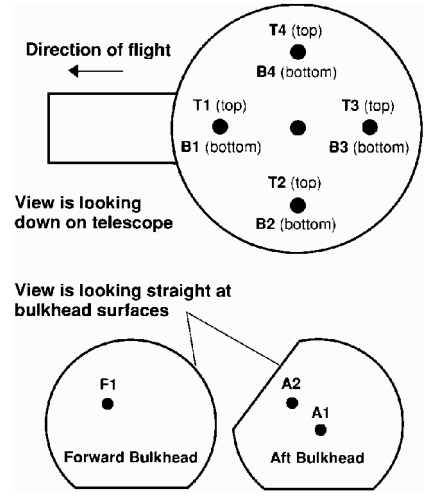

Fig. 6 Pressure tap locations of SPL on bulkheads and telescope, listed in Table 1, at wind-tunnel conditions.

Table 1 Computed and experimental SPL on telescope and bulkheads at pressure tap locations shown in Fig. 6

Location	CFD result, dB	Experiment, dB
T1	127.9	135.5
T2	137.7	135.0
T3	136.0	130.9
T4	131.5	134.8
B1	126.4	133.1
B2	127.1	133.2
B3	127.1	133.8
B4	126.5	133.3
A1	133.1	138.5
A2	134.8	137.1
F1	128.0	139.4

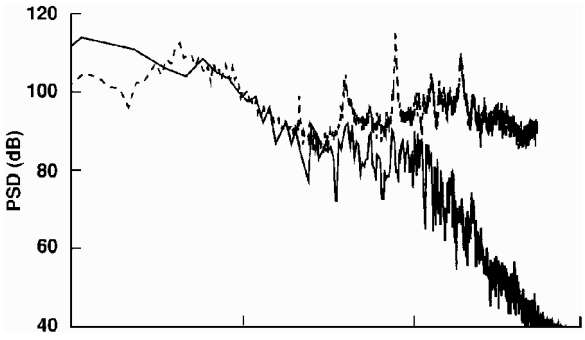

Location on forward bulkhead at F1

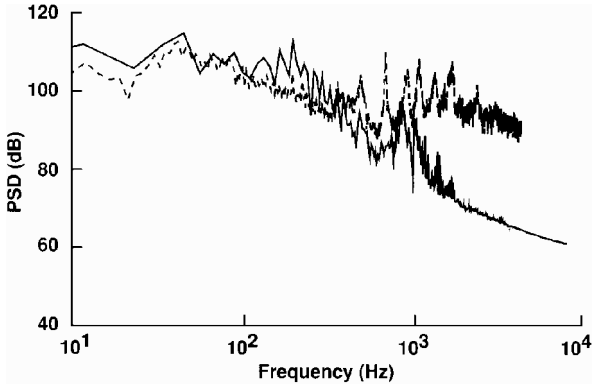

Location on aft bulkhead at A2

Fig. 7 Spectra of unsteady pressures on bulkheads at wind-tunnel conditions. ——, CFD result and – – –, experiment.

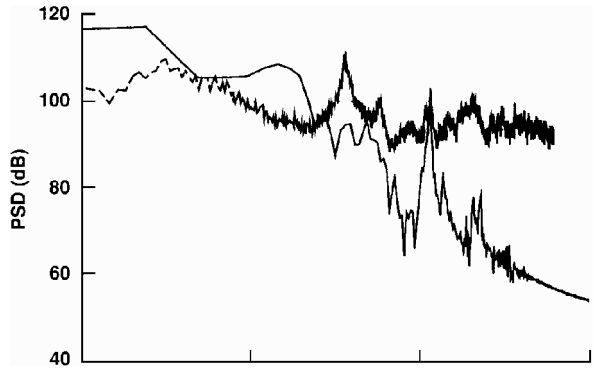

At location T4

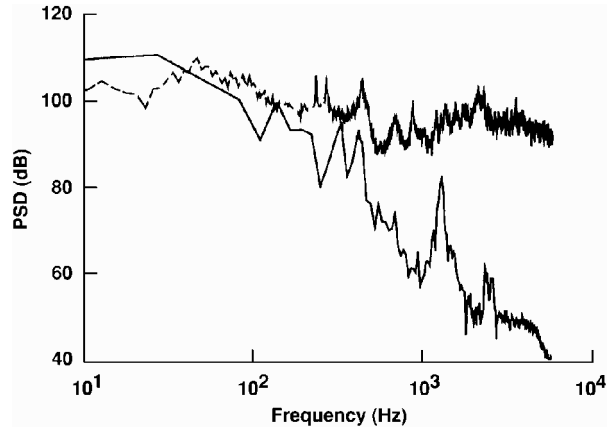

At location B4

Fig. 8 Spectra of unsteady pressures on telescope surface at wind-tunnel conditions. Telescope primary mirror—W-T case: ——, CFD result and – – –, experiment.

plots of unsteady surface pressures at some of these locations, shown in Figs. 7 and 8, reveals that the CFD calculations are in general agreement with experiments only in the frequency range of 400–1100 Hz. The spectra from CFD calculations are computed from a record containing 1923 data points and zero-padded to 2048 points. The unsteady data were stored at every 25 time-step intervals. The Welch windowing function[29] is applied to compute spectra.

The level of power spectra predicted by CFD calculations, even in this frequency range of 400–1100 Hz, is somewhat low compared to the experimental measurements. However, the major peaks of spectra are well captured, particularly the frequencies around 400, 750, and 1000 Hz. Although these frequencies are in general agreement with experimental data in this range, the low- and high-frequency contents of the spectra are not well resolved in the CFD calculations and do not agree with experiments. The spectra show a rapid falloff at high frequencies due to inadequate resolution of high-frequency waves above about 1100 Hz primarily due to numerical dissipation, a feature of the flow solver. The poor resolution of spectra at low frequencies is due mainly to the brevity of the length of CFD data trace. The net effect is underprediction of the net energy contained in these spectra and consequently in the values of SPL shown in Table 1. As mentioned before, the wind-tunnel walls are not included in the CFD calculations. Besides, there are some small differences in the cavity and telescope geometry between experimental and CFD models. In addition to the data shown in Figs. 6–8, spectra and SPL also are determined for various other locations on the bulkheads, telescope, and other cavity surfaces including aperture and are reported elsewhere.[28] The spectra and SPL also are calculated at the same locations for full-scale cruise flight condition. A comparison of W-T SPL scaled to full-scale cruise flight condition with that determined from cruise flight calculation shows a very good comparison of the two results. The scaling of SPL from W-T conditions to F-F cruise flight produces sound pressure levels that are 11 dB lower than the W-T values. The difference in length-scales and freestream conditions translates to this lower SPL in cruise flight.

The pressure on the primary mirror of telescope is highly unsteady compared to that on the bottom of the telescope tub. This is because the bottom of the tub is immersed in relatively stagnant air where the pressure profiles (time histories) are nearly identical at all locations, with very little fluctuation present in them. The spectra presented in Fig. 8 at sample locations T4 and B4 on the telescope show a behavior similar to that on the bulkheads, where the dominant frequencies (750 and 1000 Hz) appear to be reasonably well captured despite spectra levels much lower than the experiment. The spectra at B4 on the bottom of the tub shows a much steeper falloff compared to the one at T4 on the top. Time-varying loads and moments also have been calculated for the telescope and reported elsewhere.[28] Comparison of loads and moments for full-scale cruise flight conditions and wind-tunnel CFD results scaled to full-scale cruise flight show very good agreement. The time-averaged drag of the telescope is negative, consistent with the observation that the pressure on the aft bulkhead surface is higher than the rest of the cavity. Mean and rms values of telescope moments about aircraft axes and also about the telescope air bearing are reported elsewhere.[28] The air bearing assembly, mounted forward of the instrument in the aircraft, supports the telescope weight. The air bearing assembly isolates the telescope bay from the pressurized sections of the aircraft. The moments also have been calculated about a coordinate system fixed to the telescope frame of reference shown in Fig. 9. This axis system is

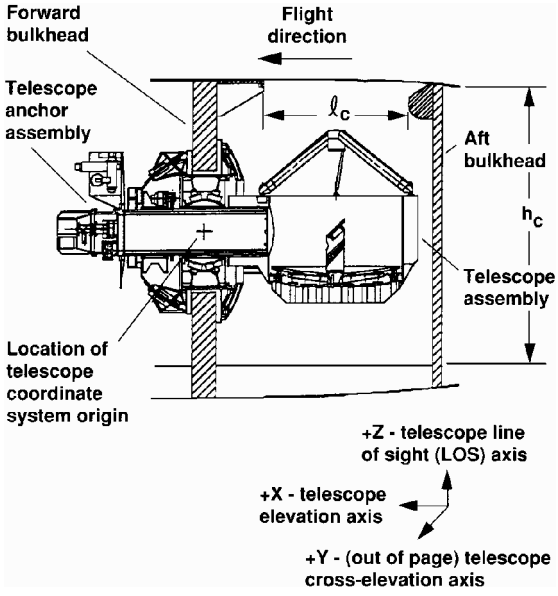

Fig. 9 Telescope coordinate system fixed to the telescope reference frame.

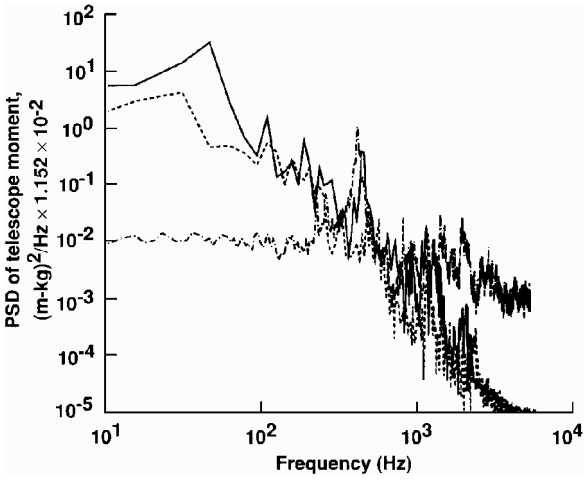

Fig. 10 Comparison of computed and experimental telescope moments about cross-elevation axis at wind-tunnel conditions. Telescope moment about cross-elevation axis: ——, CFD result at W-T condition; – – –, CFD result at F-F scaled to W-T condition; and – – –, experiment.

parallel to the aircraft axes when the telescope is at 90-deg elevation angle.

Figure 10 shows a plot of computed and experimental spectra of telescope moments about the cross-elevation axis. Two sets of CFD data are presented: One corresponds to cruise flight results scaled to wind-tunnel model conditions and the other to the wind-tunnel conditions. These two sets of CFD results, as before, are in general agreement with experimental results of moment only in the frequency range of 400–1100 Hz. The low- and high-frequency contents of spectra are not well resolved, for the same reasons cited above. The dominant frequencies around 400, 750, and 1000 Hz seem to be in good agreement with experimental data, although the level of CFD spectra is underpredicted. The good agreement of the two CFD results with each other confirms the scaling laws used to be correct.

Determination of drag increment due to open-cavity environment is one of the key objectives of the CFD investigation. Accurate determination of drag force from CFD predictions is, in general, subjected to uncertainties in gridding, grid resolution, turbulence model, and complexity of the geometry, accuracy of flow solver, etc. This is particularly true in the framework of overset grids. Only recently have tools necessary to properly account for the overlap regions of adjacent grids become available.[30] In essence, the method locates the overlap regions of neighboring grids and generates a composite surface grid, called a zipper grid, which consists of nonoverlapping quadrilaterals and triangles. Using this tool, zipper grids were constructed in the overlap regions of the present multigrid system. Force and moment coefficients then were determined. The detailed drag breakdown by individual components is reported elsewhere[28] for the complete aircraft with and without cavity. In summary, the CFD-predicted drag coefficient for clean (no-cavity) full-scale Boeing 747-200 aircraft in cruise flight is $C_D = 0.0304$, and the flight-test value for the same is 0.027 at a $C_L = 0.5$ and 0.0327 at a $C_L = 0.6$. The increase in drag coefficient due to the open cavity, in terms of equivalent flat-plate drag, is 0.42 m^2 in cruise flight.

To get more confidence in the CFD drag numbers, the drag coefficient was determined for the empennage only for the clean aircraft and that with cavity and compared with experiments. The experimental determination of drag coefficient for this section was done by two independent methods,[17] and they both are in very good agreement with each other. Again, the drag increase due to open cavity is expressed in terms of equivalent flat-plate drag. The increase in drag coefficient so determined from CFD calculations (0.286 m^2) is in excellent agreement with the experimental value (0.295 m^2) at wind-tunnel conditions.

Conclusions

A CFD investigation was undertaken to evaluate the SOFIA aircraft design issues including cavity noise. The investigation also has aided the design of a telescope configuration. CFD clearly has played a major role in generating information that is hard to measure in a wind-tunnel test. In particular, the information generated about the drag, increase in drag due to open cavity, and telescope forces and moments at both wind-tunnel and full-scale cruise flight conditions has been invaluable. Future work will improve model fidelity and extend unsteady results to the lower-frequency domain.

Acknowledgments

The valuable help by Chris Atwood in the beginning stages of this research is greatly appreciated. Useful discussions with Steve Klotz and Danny Machak also are appreciated.

References

[1] Atwood, C. A., "Navier-Stokes Simulations of Unsteady Transonic Flow Phenomena," NASA TM 103962, Aug. 1992.

[2] Rose, W., "SOFIA Wind Tunnel Data Analysis and Implications for Full-Scale Aircraft," Rose Engineering Research, TR, Incline Village, NV, Dec. 1990.

[3] Rose, W., "SOFIA—Aft Cavities Wind Tunnel Test—Pre-Test Report," Rose Engineering Research, TR, Incline Village, NV, Feb. 1993.

[4] Rose, W., "SOFIA—Aft Cavities Wind Tunnel Test—Final Report," Rose Engineering Research, TR, Incline Village, NV, Dec. 1994.

[5] Komerath, N. M., Ahuja, K. K., and Chambers, F. W., "Prediction and Measurement of Flows over Cavities—A Survey," AIAA Paper 87-0166, Jan. 1987.

[6] Srinivasan, S., and Baysal, O., "Navier-Stokes Calculations of Transonic Flow Past Cavities," *Journal of Fluids Engineering*, Vol. 113, Sept. 1991, pp. 368–376.

[7] Baysal, O., Yen, G.-W., and Fouladi, K., "Navier-Stokes Computations of Cavity Aeroacoustics with Suppression Devices," *Journal of Vibration and Acoustics*, Vol. 116, Jan. 1994, pp. 105–112.

[8] Baysal, O., and Stallings, R. L., Jr., "Computational and Experimental Investigation of Cavity Flowfields," *AIAA Journal*, Vol. 26, No. 1, 1988, pp. 6, 7.

[9] Vakili, A. D., and Wolfe, R., "Active Control of Cavity Aeroacoustics in High Speed Flows," AIAA Paper 95-0678, Jan. 1995.

[10] Rizetta, D., "Numerical Simulation of Supersonic Flow over a Three-Dimensional Cavity," *AIAA Journal*, Vol. 26, No. 7, 1988, pp. 799–807.

[11] Hankey, W. L., and Shang, J. S., "Analyses of Pressure Oscillations in an Open Cavity," *AIAA Journal*, Vol. 18, No. 8, 1980, pp. 892–898.

[12] Buell, D. A., "An Experimental Investigation of the Airflow over a Cavity with Antiresonance Devices," NASA TN D-6205, March 1971.

[13] Buell, D. A., "Airloads Near the Open Port of a One-Meter Airborne Telescope," AIAA Paper 75-71, Jan. 1975.

[14] Atwood, C. A., and Van Dalsem, W. R., "Flowfield Simulation About the Statospheric Observatory for Infrared Astronomy," *Journal of Aircraft*, Vol. 30, No. 5, 1993, pp. 719–727.

[15] Atwood, C. A., "Unsteady Fluid and Optical Flow Simulation of Transonic Aero-Windows," AIAA Paper 93-3017, July 1993.

[16]Atwood, C. A., "Selected Computations of Transonic Cavity Flows," AIAA Paper 93-3017, July 1993.

[17]Machak, D., Srinivasan, G. R., and Klotz, S. P., "Aerodynamic Characteristics of the Stratospheric Observatory for Infrared Astronomy," AIAA Paper 95-0398, Jan. 1995.

[18]Klotz, S. P., "The 747-SP SOFIA Platform: A Comparison of CFD Simulations and Wind Tunnel Experiments," MCAT, TR 95-02, San Jose, CA, April 1995.

[19]Pulliam, T. H., and Steger, J. L., "Implicit Finite-Difference Simulations of Three-Dimensional Compressible Flow," *AIAA Journal*, Vol. 18, No. 2, 1980, pp. 159–167.

[20]Buning, P. G., and Chan, W. M., "OVERFLOW User's Manual," Version 1.6al, NASA Ames Research Center, Moffett Field, CA, July 1994.

[21]Pulliam, T. H., and Chaussee, D. S., "A Diagonal Form of an Implicit Approximate-Factorization Algorithm," *Journal of Computational Physics*, Vol. 39, Feb. 1981, pp. 347–363.

[22]Baldwin, B. S., and Lomax, H., "Thin-Layer Approximation and Algebraic Model for Separated Turbulent Flows," AIAA Paper 78-257, Jan. 1978.

[23]Steinbrenner, J. P., Chawner, J. R., and Fouts, C. L., "A Structured Approach to Interactive Multiple Block Grid Generation," *AGARD Fluid Dynamics Panel Specialists Meeting on Mesh Generation for Complex Three-Dimensional Configurations* (Loen, Norway), AGARD-CP-464, 1989, pp. 8.1–8.12.

[24]Luh, R. C.-C., Pierce, L. E., and Yip, D., "Interactive Surface Grid Generation," AIAA Paper 91-0796, Jan. 1991.

[25]Chan, W. M., and Steger, J. L., "A Generalized Scheme for Three-Dimensional Hyperbolic Grid Generation," AIAA Paper 91-1588, June 1991.

[26]Benek, J. A., Buning, P. G., and Steger, J. L., "A 3-D Chimera Grid Embedding Technique," AIAA Paper 85-1523, July 1985.

[27]Suhs, N. E., and Tramel, R. W., "PEGSUS 4.0 User's Manual," Arnold Engineering Development Center, AEDC-TR-91-8, Arnold AFB, TN, Nov. 1991.

[28]Srinivasan, G. R., "Flowfield and Acoustic Characteristics of Telescope Cavity in SOFIA Platform," AIAA Paper 95-1862, June 1995.

[29]Press, W. H., Teukolsky, S. A., Vetterling, W. T., and Flannery, B. P., *Numerical Recipes in FORTRAN*, Cambridge Univ. Press, Cambridge, England, UK, 1992.

[30]Chan, W. M., and Buning, P., "Zipper Grids for Force and Moment Computation on Overset Grids," AIAA Paper 95-1681, June 1995.

R. M. Cummings
Associate Editor